MEMORANDUM REPORT BRL-MR-3922

BRL

A METHOD OF INVESTIGATING SCALES OF MOTION IN A TURBULENT WAKE

PHILLIP C. DYKSTRA
JOHN D. KUZAN

JUNE 1991

U.S. ARMY LABORATORY COMMAND

BALLISTIC RESEARCH LABORATORY
ABERDEEN PROVING GROUND, MARYLAND

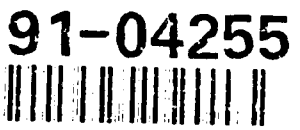

NOTICES

Destroy this report when it is no longer needed. DO NOT return it to the originator.

Additional copies of this report may be obtained from the National Technical Information Service, U.S. Department of Commerce, 5285 Port Royal Road, Springfield, VA 22161.

The findings of this report are not to be construed as an official Department of the Army position, unless so designated by other authorized documents.

The use of trade names or manufacturers' names in this report does not constitute indorsement of any commercial product.

REPORT DOCUMENTATION PAGE

Form Approved
OMB No. 0704-0188

1. AGENCY USE ONLY (Leave blank)	2. REPORT DATE	3. REPORT TYPE AND DATES COVERED
	June 1991	Final. Dec 89-Aug 90.

4. TITLE AND SUBTITLE

A Method for Investigating Scales of Motion in a Turbulent Wake

5. FUNDING NUMBERS

1L162618AH80

6. AUTHOR(S)

Phillip C. Dykstra and John D. Kuzan

7. PERFORMING ORGANIZATION NAME(S) AND ADDRESS(ES)

8. PERFORMING ORGANIZATION REPORT NUMBER

9. SPONSORING / MONITORING AGENCY NAME(S) AND ADDRESS(ES)

Ballistic Research Laboratory
ATTN: SLCBR-DD-T
Aberdeen Proving Ground, MD 21005-5066

10. SPONSORING / MONITORING AGENCY REPORT NUMBER

BRL-MR-3922

11. SUPPLEMENTARY NOTES

12a. DISTRIBUTION / AVAILABILITY STATEMENT

Approved for public release; distribution is unlimited.

12b. DISTRIBUTION CODE

13. ABSTRACT *(Maximum 200 words)*

Knowledge of the scales of motion in the flow around a body is important for accurate turbulence modeling in computational fluid dynamic calculations. Useful data can be measured in wind tunnel experiments, but often not for the free flight conditions of interest. This report examines the possibility of determining such information from shadowgraphs taken in a ballistic range. The application of digital scanning machines and spatial correlation interrogation to shadowgraphs are described. One method of analyzing a shadowgraph to extract information about turbulence structures in the flow field is discussed. Results are shown for the analysis of two regions in the wake of a projectile. This method might be used to quantify the effects of various projectile modifications on a turbulent structure, for example the introduction of a base burn unit.

14. SUBJECT TERMS			15. NUMBER OF PAGES
Turbulence Shadowgraphs Wake Flow	Image Processing		35
			16. PRICE CODE

17. SECURITY CLASSIFICATION OF REPORT	18. SECURITY CLASSIFICATION OF THIS PAGE	19. SECURITY CLASSIFICATION OF ABSTRACT	20. LIMITATION OF ABSTRACT
UNCLASSIFIED	UNCLASSIFIED	UNCLASSIFIED	SAR

NSN 7540-01-280-5500

Standard Form 298 (Rev 2-89)
Prescribed by ANSI Std 239-18
298-102

INTENTIONALLY LEFT BLANK.

Table of Contents

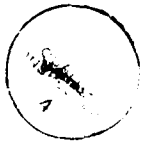

INTENTIONALLY LEFT BLANK.

List of Figures

INTENTIONALLY LEFT BLANK.

List of Tables

INTENTIONALLY LEFT BLANK.

1 Introduction

In the 1940's, Kovasznay [1] was interested in obtaining measurements of fluid turbulence quantities in the wake of artillery projectiles. His technique used duplicate slides of a spark range shadowgraph (see Section 3) and a light source to perform a spatial correlation of the light intensity in the wake imaged on the shadowgraph. He then used the theory of Taylor [2] to obtain statistical properties of the three dimensional density fluctuations in the wake from the two dimensional light intensity fluctuations in the shadowgraph. This was a slow process. With the use of digital scanning devices and computers, the process is much quicker. This report shows the results of using modern equipment to interrogate a spark range shadowgraph with Kovasznay's technique.

2 Background

Ballistic ranges and wind tunnels have been used for several decades to determine the force and moment coefficients that describe the stability and the motion of a projectile in free flight. For many years, these facilities provided the only means of determining those coefficients. In the past ten years, computational fluid dynamics has developed enough to allow the value of these coefficients to be determined from a computer solution to the Navier-Stokes equations. Nevertheless, the computer solutions need information about the viscous layer of the flow field surrounding the projectile, especially in transonic flight.

Computer solutions to the Navier-Stokes equations generally use one of two closure schemes: an algebraic model to define a turbulent viscosity or a model of the turbulent kinetic energy production and dissipation. Both models benefit from experimental flow field data. For example, the "Baldwin-Lomax" model [3] is used successfully in computational fluid dynamics for closure to the Navier-Stokes equations. The Baldwin-Lomax model takes advantage of the Prandtl-Van Driest formulation for the turbulent viscosity. In this model, the mixing length, ℓ, varies with distance from a boundary (or wall) according to:

$$\ell = \kappa y[1 - \exp(-y^+/A^+)]. \tag{1}$$

In this equation, κ and A^+ are constants, y is the dimensional distance from the boundary, and y^+ is a non-dimensional distance from the boundary. The mixing length translates to a physical length within the flow field, namely the size of the eddies that are transporting the bulk of the momentum. Experimental measurements of the size of these eddies would benefit the modeling. Similarly, measurements of the turbulent energy spectra in the flow field help the production-dissipation models of turbulence.

The computer solutions calculate the velocity and pressure fields in the boundary layer surrounding a projectile in flight. Once the pressure at the surface of the projectile is calculated, the forces and moments (and, finally, the coefficients used in trajectory and stability analysis) can be calculated. While in a wind tunnel, techniques such as hot wire anemometry or laser-Doppler velocimetry measure velocities in the flow field, the same is generally not true for ballistic ranges. Similarly, pressure measurements in the flow field can be made in a wind tunnel, but are not made routinely in ballistic ranges. Instead, ballistic ranges are used to find the position of a projectile at a certain time and then, with the equations of motion, that information is used to calculate the ballistic coefficients.

Detailed experimental information about the flow field around a body is usually only available from wind tunnel measurements, and not from ballistic ranges. However, wind tunnel measurements of velocity and pressure fields are not ideal, since the projectile is not in free flight and the Reynolds number can be significantly different from free flight conditions. Wind tunnel measurements can also be subject to unknown disturbances from the walls and mounting structures. Thus, any technique for extracting flow field information from the ballistic range would be of use to those who model the flow field on the computer.

The point-to-point statistical record of the velocity fluctuations in a turbulent flow field available from laser-Doppler velocimetry is nearly impossible to obtain in a ballistic range; even if one measurement could be made, the number of firings required for an ensemble average would be prohibitive. Large field optical techniques would be of great interest if they were able to capture the instantaneous two dimensional flow field around a projectile. In this way, an ensemble average might be made in ten or so firings. The technique discussed in this paper is very far from being able to give a quantitative picture of the flow field surrounding the projectile. Nevertheless, the use of simple shadowgraphs and computers suggests that more information can be squeezed from the ballistic range that is of importance to computational modeling.

3 The Shadowgraph

Shadowgraphs can be produced in the Transonic Range at the Ballistic Research Laboratory. It is a 207 meter long building with a 6 meter square test section instrumented with 25 orthogonal shadowgraph stations, as described by Rogers [4]. In addition to the orthogonal shadowgraph stations, it is possible to obtain a direct photograph of the flow field surrounding the projectile through the use of a mosaic station. This station consists of a platform positioned near the line of flight of the projectile and covered with sheets of photographic film. (The mosaic is a direct shadowgraph; the orthogonal stations produce indirect shadowgraphs, i.e. the shadowgraph image is projected onto a screen and the screen is photographed. See Rogers for the details.) When the projectile is above the platform, a light source is triggered to obtain the shadowgraph. This composite picture generally magnifies the flow field. The mosaic station for the present work was placed at a distance of 122 meters from the gun; Figure 1 is a schematic of the station.

Figure 2 shows a shadowgraph obtained from the mosaic station; a schematic is presented in Figure 3 to clarify what is shown in the shadowgraph. The projectile in the shadowgraph is an 155mm, M864 Base-Burn projectile; as shown in the schematic, only a small portion of the projectile base is imaged. There is some gas injection shown in the shadowgraph, although the propellant in the M864 has not reached a steady-state burn.

Shadow patterns on the shadowgraph are produced by a redistribution of the intensity of the illuminating spark light source. The rays of light are deflected as though there were small lenses in the wake region; hence, the formation of a "shadow" depends on the changes in deflection, not on the actual value of the deflection angle. For small angles of deflection,

$$\Delta x = l\theta \tag{2}$$

where the displacement of the light ray on the shadowgraph is Δx, l is the distance between the centerline of the wake and the shadowgraph, and θ is the angle of deflection at the wake.

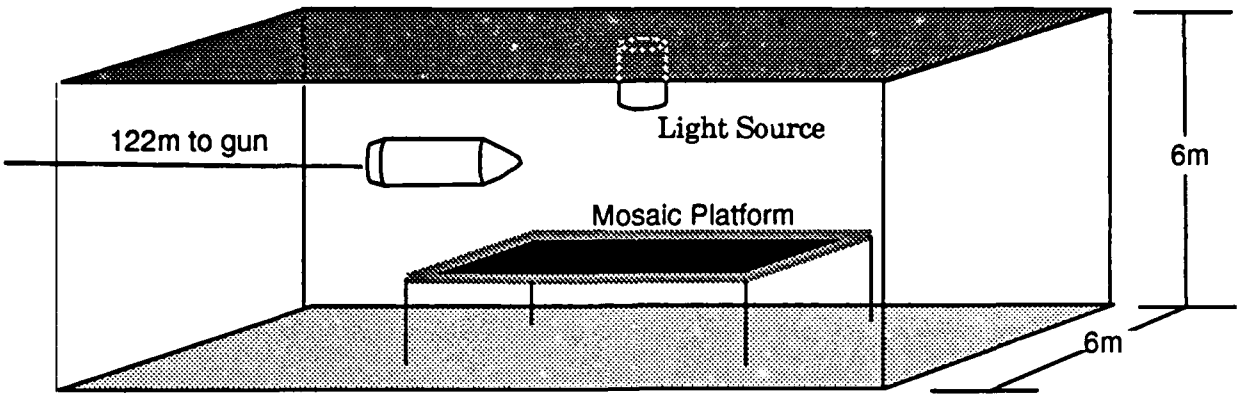

Figure 1: Shadowgraph Arrangement in the Transonic Range

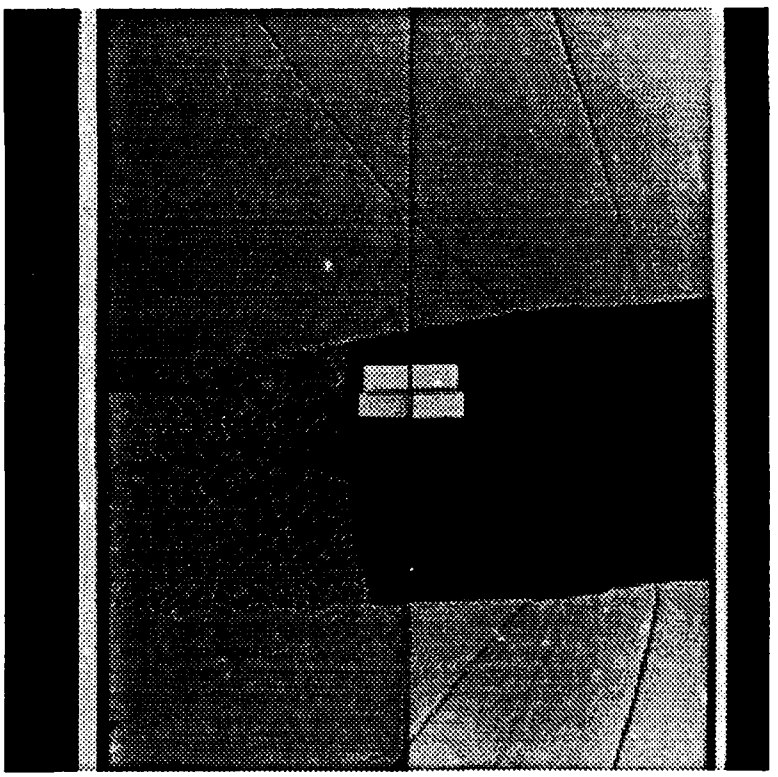

Figure 2: Schematic of Shadowgraph of M864 Base-Burn Projectile with Gas Injection

Uniform deflection would move the rays of light uniformly; only changes in θ will result in a varying Δx at the shadowgraph. These changes in Δx correspond to local variations of the light intensity on the screen, and thus appear as lighter and darker regions on the shadowgraph.

Density variations in the wake account for the effective lenses since, from the empirical law due to Gladstone and Dale [5],

$$\frac{\delta}{\rho} = K \quad \text{or} \quad n = \rho K + 1 \tag{3}$$

where K is the Gladstone-Dale constant, δ is equal to $n - 1$ (n is the refractive index[1]) and ρ is the density of the gas. For air, the density varies with the temperature, T, and the pressure, p, according to:

$$\rho = \rho_0 \frac{T_0}{T} \frac{p}{p_0} \tag{4}$$

where the zero subscript refers to an initial value. Hence, variations of the pressure or temperature in the wake of the projectile result in density variations in the wake, and, thus, refractive index variations. This makes shadows on a surface opposite the light source illuminating the wake.

If a density fluctuation creates an apparent convex lens, then there is the possibility that the light rays passing through the apparent lens will focus before they reach the film. In this case the resulting shadowgraph will not have a one-to-one correspondence between its shadows and the density fluctuations. The shortest focal length that could result from the shadowgraph used in this study can be determined from the lens maker's equation:

$$\frac{1}{f} = \delta \left(\frac{1}{r_1} - \frac{1}{r_2} \right) \tag{5}$$

where r_i are the radii of curvature of each side of the lens and f is the focal length (positive if on the real side of the lens, negative if on the virtual or image side). The worst case would occur with a flat surface on the incoming ray side of the lens and a radius of the resolution of the film (300 lines per millimeter) on the outgoing side. Equations 3 and 4 can be used to determine the change in the refractive index of air given that the pressure is twenty per cent lower in the wake than in the free stream (a worst case). With these conditions, the focal length is about 2 meters. The wake was about one meter away from the film in this study; therefore, it is assumed that a one-to-one correspondence exists between the density fluctuations and the record on the shadowgraph.

A simple relation holds for the deflection angle of the light rays with changes in refractive index, namely:

$$\theta = - \int_{-z}^{+z} \frac{\partial \delta}{\partial x} dz \tag{6}$$

where z is the direction normal to the shadowgraph and the wake is $2Z$ thick. (The coordinate system is shown in Figure 4.) Thus, summing all the variations in refractive index through the thickness of the wake yields the resulting angle of deflection of the incoming ray of light.

[1] The refractive index is the ratio of the velocity of light in vacuum to the velocity of light in the given medium. The ratio of the difference in velocities to the velocity in the medium is the value of δ.

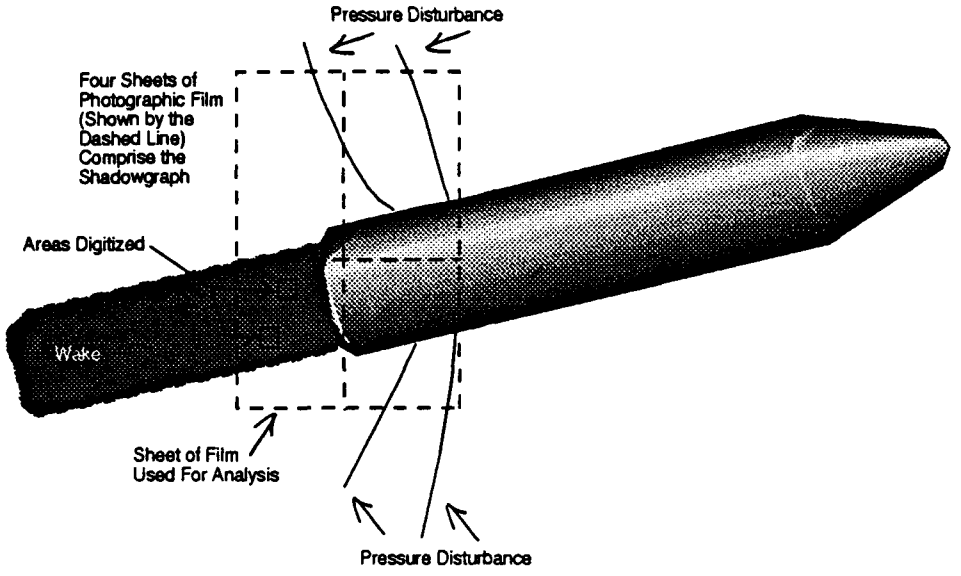

Figure 3: Shadowgraph and Schematic of M864 Base-Burn Projectile

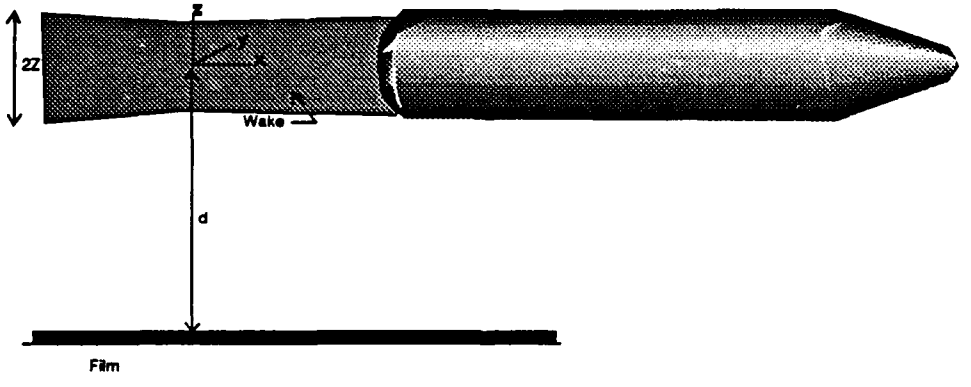

Figure 4: Distance and Sign Conventions

The first step in analyzing the shadowgraph is to determine the relationship between the intensity of the light recorded on film (the illumination) and the density fluctuations in the wake. The change in illumination, I, (energy/area/time) is in proportion to the rate of change of the deflection of light rays with distance [6]:

$$\frac{\Delta I}{I} \propto \frac{d\theta}{dx}. \tag{7}$$

This is true as long as the refractive index gradients are not too large, as is the case for shadowgraphs of the wake of projectiles. The same is not necessarily true for flames. This can have consequences for powered projectiles, such as rocket-assisted or base-burn projectiles.

Combining Equations 3, 6, and 7 and taking three dimensions into consideration yields:

$$\frac{\Delta I}{I} = -\frac{lK}{\rho_0}\int_{-z}^{+z}\frac{\partial^2\rho}{\partial x^2}+\frac{\partial^2\rho}{\partial y^2}\,dz = -\frac{lK}{\rho_0}\int_{-z}^{+z}\nabla^2\rho\,dz \tag{8}$$

where l remains the distance from the centerline of the wake to the shadowgraph, K is the Gladstone-Dale constant, ρ_0 is the air density in the free stream, ρ is $\rho(x,y,z)$ and y is the direction in the same plane as and perpendicular to x. At this point it is convenient to define a dimensionless parameter that indicates the illumination on the shadowgraph:

$$F(x,y) \equiv \frac{I_0 - I(x,y)}{I(x,y)} = \frac{\Delta I}{I} \tag{9}$$

where the zero subscript refers to the undisturbed illumination of the shadowgraph. Function F can be negative; it is not a gray scale.

4 Spatial Correlation

The correlation coefficient of the density fluctuations in the wake of a projectile was determined by Kovasznay [1] using an optical technique. He made a duplicate of the shadowgraph transparency, placed the duplicate behind the original, and used a traversing mechanism to move one shadowgraph with respect to the other in the plane of the shadowgraphs. Using a light source and a photodetector, he could measure the transmittance through both shadowgraphs resulting from different separations (the distance between a corner of one shadowgraph and the same corner of the other). This formed the local correlation coefficient, J, from a separation, s:

$$J_T(s) = \int I_{\text{int}}\,T(\mathbf{x})T(\mathbf{x}+s)\,d\mathbf{x} \tag{10}$$

where I_{int} is the intensity of the light source and $\mathbf{x}$ is the vector locating position in the overlapping areas of the shadowgraphs. Term T is the transmissivity of the shadowgraph, which is related to $F(x,y)$. This correlation coefficient for the two dimensional shadowgraph was then related to the three dimensional density fluctuations by Equation 8:

$$J_T(s) \propto \int\left[\int_{-z}^{+z}\nabla^2\rho\,dz\int_{-z'}^{+z'}\nabla^2\rho\,dz'\right]. \tag{11}$$

The local correlation of the density fluctuations is defined as:

$$J_\rho(s) = \int \rho(\mathbf{X})\rho(\mathbf{X}+s)\,d\mathbf{X} \tag{12}$$

where $\mathbf{X}$ is a three-dimensional position vector, so that Equation 11 can be rewritten as:

$$J_T(s) = C\int_{-Z}^{+Z}\int_{-Z'}^{+Z'}\left[\nabla^2\right]^2 J_\rho(s)\,dz'\,dz \tag{13}$$

where C is a constant. Since J_ρ is a function of the displacement s only, and ρ is statistically homogeneous [7], the Laplacian is now:

$$\nabla^2 = \frac{1}{s}\frac{\partial}{\partial s}\left(s\frac{\partial}{\partial s}\right). \tag{14}$$

By defining a new variable $\xi = z - z'$, Equation 13 becomes:

$$J_T(s) = C\int_0^{2Z}(2Z-\xi)\left[\nabla^2\right]^2 J_\rho(s)\,d\xi \tag{15}$$

If the thickness of the wake is much larger than the largest turbulent scales that can be resolved in the correlation, then the length $2Z$ is effectively infinite. In this case, Equation 15 can be solved by inverse Fourier transform.

5 Discrete Interrogation of the Shadowgraph

Another technique for spatial correlation of the shadowgraph is to discretize the illumination with the use of an optical scanning device. In this operation, the shadowgraph is divided into small square areas, ($A_{i,j}$), as shown in Figure 5. The illumination in a portion of each area is averaged; the value of the average is represented by $I_{i,j}$. Figure 5 depicts the portion used in the averaging process.[2] An area's average in this work could take on integer values between zero (for no illumination) and 255 (for 100% illumination).

Local correlation of the illumination can be represented by:

$$J_I(a,b) = \left(\sum_i\sum_j I_{i,j}\,I_{i+a,j+b}\right) \tag{16}$$

where a and b are the number of row and column separations. Hence, the duplicate shadowgraph technique described above can be replicated by a "shift and multiply" technique on the computer which, if done in Fourier space, is very fast.

The density field in the wake can be transformed using the following expansion:

$$\rho(x,y,z) = \sum_{|p|\le\frac{P}{2}}\sum_{|q|\le\frac{Q}{2}}\sum_{|r|\le\frac{R}{2}} g_{pqr}\,G\left(\frac{px}{\lambda_x}+\frac{qy}{\lambda_y}+\frac{rz}{2Z}\right). \tag{17}$$

In this equation, P, Q, and R are the number of Fourier modes in the x, y, and z directions, function g is the spectrum of the density, and $G(\alpha) \equiv \cos(\alpha) + \sin(\alpha)$. Terms λ_x and λ_y are

[2] $I_{i,j}$ is obtained from a subset of $A_{i,j}$ due to the hardware being used (see next section for details).

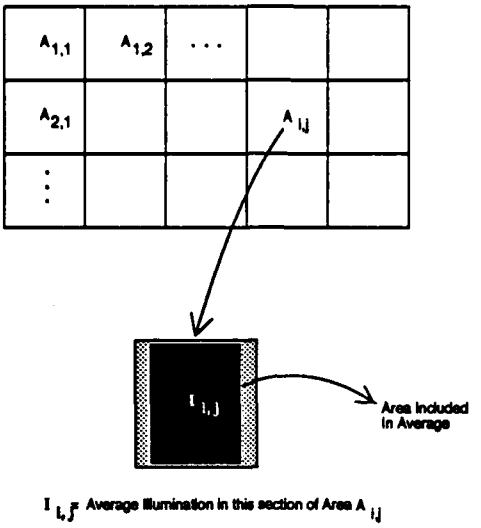

Figure 5: Schematic of Discrete Values of the Illumination on Shadowgraphs

the lengths of the wake as imaged on the shadowgraph in the subscripted direction. When this expansion is substituted into Equation 8, the factor $\frac{\sin rZ}{r}$ results from the differentiation. In the limit of $Z \to \infty$ (which is reasonable for the shadowgraph where the scale of the turbulence patterns is much smaller than the thickness of the wake) and treating the summation over r as infinite, then:

$$\int_{-\infty}^{+\infty} \left(\frac{\sin Zr}{r} dr \right) = \pi \tag{18}$$

and the final result is:

$$F(x,y) = -\frac{\pi l K}{\rho_0} \sum_{|p| \le \frac{P}{2}} \sum_{|q| \le \frac{Q}{2}} \left(\frac{p^2}{\lambda_x^2} + \frac{q^2}{\lambda_y^2} \right) g_{pq0}\, G\left(\frac{px}{\lambda_x} + \frac{qy}{\lambda_y} \right). \tag{19}$$

6 Equipment

The digital scanning device used was an Eikonix Model 1412 Digital Imaging Camera, built by the Eikonix Imaging Systems division of Kodak. Since this was the first project in the BRL to attempt to make quantitative measurements with this device, considerable effort was put into the calibration of the equipment and the determination of error thresholds for the system. Several errors and important omissions were found in the documentation from Eikonix; hence, the following is presented as an aid to future users of this device.

The camera consists of a 55mm f/2.8 Nikon lens in front of a 4096 element charged coupled device (CCD) array. This one-dimensional CCD array can be stepped through 4096 positions allowing up to a 4096x4096 pixel scan. The elements of this array are five microns wide by seven microns high, with a two micron gap between each element in the five micron direction. Each sample, or pixel, is quantized by a 12-bit analog to digital (A/D) converter. The finite size of each pixel means that the output of the scanner is a point sampling of the input image after a rectangular "box car" filter has been applied.

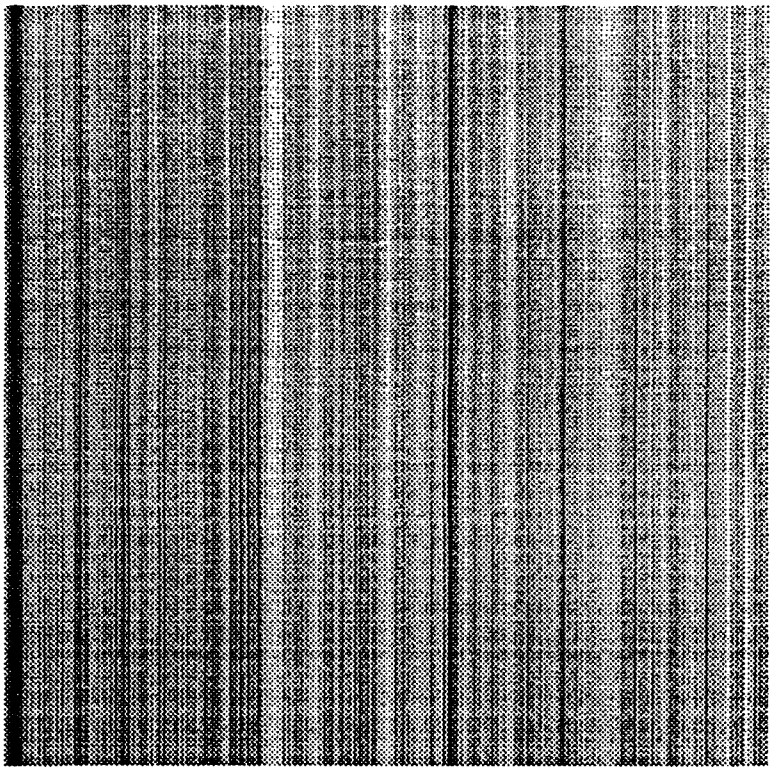

Figure 6: Detail of Uncalibrated Scanner Output

The object being scanned can either be transmissive (e.g. photographic negatives) or opaque (e.g. prints). A fluorescent light table is used for the former case, while four tungsten lamps provide top lighting for opaque objects. The exposure is controlled by both the f-stop of the lens and the "integration time" of the CCD array, which is discussed below. A programmable filter wheel allows for color scanning via red, green, and blue filters; but, only gray scale was used and discussed in this report.

Since the spacing of the CCD array is fixed, the resolution of a scan is controlled by the distance of the camera above the scanned surface. At its closest focus, the camera yields approximately a 55mm wide scanning area over the 4096 element array, or a 13.4 micron sample spacing (1892 samples per inch). Higher resolution could be obtained by changing lenses on the camera (Eikonix offers an optional 105mm lens). A practical limit for the largest single area that can be scanned is approximately 1 meter side to side, which yields a sample spacing of 244 microns (104 samples per inch). For the 55mm lens, the width of the scanned area was found to be related to camera position by:

$$\text{scan width} = 4.95\ \text{camera position} + 13\text{mm} \tag{20}$$

The camera is connected to, and controlled by, a Sun Microsystems 3/280 computer *via* an IEEE-488 bus interface. The light sources, camera distance, focus, and f-stop are controlled manually. Scanning area, exposure, CCD array normalization, etc. are computer controlled. Data can be transferred to the computer as either 8 or 12 bits per sample (in the former case, the lower 4 bits of the A/D converter are ignored).

Naive use of the scanner can result in fairly substantial errors. Figure 6 shows a contrast enhanced result of a scan of a uniform white field. The brightness variations have been exaggerated by a factor of fifteen. The lines running vertically through the image result from the non-uniform response of the CCD array elements. The horizontal lines in the image result from brightness variations in the light source during the scanning process. The following discussion shows that corrective measures can be taken to reduce, but not eliminate, both of these errors.

Each element of the CCD array acts as an integrator of the incoming light. Between the time that an element is cleared or "set to zero" and the time that it is sampled by the A/D converter it will sum up the illumination that falls on it. This time interval is called the "integration time." Each element of the array responds linearly to the incident illumination. However, the constants of this linear equation are different for every element, and will vary with temperature.

Ideally, if an element received no light during its integration time the sampled output would read zero. In practice, each element will yield some small non-zero value referred to as the "dark current." If exposed to equal amounts of light, the sampled outputs of every element should read the same; but, due to sensitivity variations from element to element. this does not happen. To "normalize" the response of the array, a bias and gain value should be computed for every element of the array and then scanned values should be corrected by these factors.

The Eikonix camera contains bias and gain buffers which can be loaded with these correction factors. This calibration procedure involves exposing the array to black (e.g. with the lens cap on) to find bias values, and then exposing the array to a uniform white field to find gain values. To achieve the best possible uniform white, the authors suggest fully defocusing the camera over either the cleaned surface of the light table (for transmissive scans) or a plain white sheet of paper (for reflective scans). Observation of a pin hole light source showed the point spread when fully defocused to be approximately one twentieth of the entire scanning area.

Variation in the light source during integration can also be a problem and was the source of the horizontal lines in Figure 6. The major source of this variation is the 120Hz "flicker" of the lights caused by the AC power supply. It is important that the CCD array be exposed for an integral multiple of this flicker time, otherwise the amount of light received during the integration time will depend on the phase of the lights at the instant each scan line exposure begins. The manual makes the erroneous claim that the flicker of the tungsten lights is somehow taken into account by the camera. While the rather massive filaments and the low operating voltage of the tungsten lamps reduces this problem, flicker is still present. A photocell was used to measure this light variation and was found to be slightly over two per cent peak to peak.

The flicker of the fluorescent light table is extreme, since the light almost completely shuts off between cycles. Getting the correct integration time is critical.[3] Given the potential asymmetries in the fluorescent discharge cycle, the flicker cycle rate should be treated as

[3] There are several incorrect or confusing formulas for the integration time in the manual. For the model 1412 camera it is simply

$$integration\ time = \frac{clock\ rate\ count * integration\ time\ count}{6}\ \text{microseconds}$$

60Hz (16.67 msec). There was one other low frequency error associated with the fluorescent light table that could be seen with the naked eye and is impossible to remove; this error results from unstable oscillation of the gas plasma.

One additional error associated with the Eikonix camera was found. After calibrating the bias and gain tables, individual scan lines still show a systematic offset between gray values reported for even and odd pixels. The CCD array used in the camera is designed where even and odd elements are separated into two distinct output stages. It was not determined whether this error resulted from a flaw in the automatic calibration sequence, or from an instability in the CCD device. The end result was a small noise component at the Nyquist rate (wave number of one half sample) in the horizontal direction.

For the scans in this report, prints of the shadowgraph were used with the reflective tungsten lighting. An integration time of 33.333 msec was used. From one scan to the next, sample values varied by about five per cent. This seems disappointingly high, but is of the same order as the quantization noise for our images.

7 Results

The shadowgraph of Figure 3 was digitized; the result is shown in Figure 7. This figure is from the lower left of the four plates in the shadowgraph configuration. The dark area at the upper right of the shadowgraph is the base of the projectile. Two areas were selected from this shadowgraph for statistical evaluation and are shown by the boxes in the figure. Area one is the "course grained" region near the base of the projectile, and area two is in the finer grained region to the lower left. Each of these areas were digitized with nearly the maximum resolution of the scanner and contain 4096 by 4096 samples. Each sample is 14.6 microns on the photographic print. Careful measurement of the projectile in the figure showed that the shadowgraph was magnified by a factor of 1.63. The projectile was traveling at a Mach number of about 1.2.

Detailed pictures of these two areas are shown in Figures 8 and 10. Each of these pictures covers an area of 36.2 mm on a side; each sample was thus 8.84 microns on a side (113 pixels/mm). Statistical quantities, showing the distribution of gray values among pixels, are shown in Table 1. The associated histograms are shown in Figures 9 and 11. The statistical quantities are similar in both areas, although area one is skewed to a greater extent. Both areas use less than half of the gray scale resolution available. This would suggest that an additional 6 dB of signal to quantization noise ratio (SNR) might be obtained by either a higher contrast print, or a better scanner exposure.

Figures 12 through 15 show the results from shift and multiply in one row or column of the digitized areas. These are normalized such that the maximum is unity in the unshifted position. The mean value for the entire area has been subtracted. At larger values of shift, less samples are included in the autocorrelation estimate. As a result, the variance of the estimate goes up. To avoid misinterpretation of this data, the biased autocorrelation estimate is shown.

After the initial decrease from the unshifted position, all four correlations display a sinusoidal variation for about 20 mm. Periodicity in these results is an indication of the size of the scales of motion in the wake. These figures show that the most significant scale that is resolved from this process has a length of about one millimeter; this is the same length that

Kovasznay[1] found in his work. This is based on the first zero crossing in each of the figures, since this is the distance at which patterns on the shadowgraph are uncorrelated. Because the autocorrelation was performed using a zero-based average for the gray value, negative values of the autocorrelation are possible and indicate the distance at which patterns with gray values below the average are correlated with those above. Area two has a somewhat higher frequency of the variations than area one, and this is consistent with the notion of a finer grain in the turbulent structure of area two.

Figures 16 through 19 are the averages of the autocorrelation estimates of all the rows and all the columns in the two areas. The autocorrelation approaches zero near a separation distance of one millimeter in all four figures. In the average, the periodicity that was so apparent in the single row or column autocorrelation has been smoothed. Now the autocorrelation appears to be that for a random function: rapid decay from a maximum value to zero. This shows that while in any given row or column there are particular frequencies that are dominant, those frequencies change a short distance away. Averaged over the entire area, a broad range of frequencies (or length scales) are present in a continuous manner. This is consistent with the dynamics of turbulent wake flow.

The results of the two-dimensional autocorrelations are shown in Figures 20 through 23; both a contour plot and a gray scale image are presented. The values of the autocorrelation are indicated on the contour plot; the gray scale image shows positive values as levels of gray, with black indicating values of zero or less. These were computed over an area of 512 square pixels; the shift was 512 pixels in both the column and row directions. The 512 pixels chosen were from the lower left corner of each area. The local minimum in area one occurs about 1.5 mm from zero separation; it is skewed such that it is farther from zero in the column direction. In area two, the skew is toward the row direction; however, the magnitude of the distance is once again near 1.5 mm. Area two appears to have some coherence along the diagonal (see Figure 10) and this shows up in the two-dimensional correlation as a diagonal streak of white after the local minimum.

Rotational correlations give an indication of length scale in the wake, and these are shown with five degrees of rotation in Figures 24 and 25. Rings form about three millimeters from the center of the picture, and these rings have a spacing of about one millimeter. Again, this suggests the correlation of density fluctuations in a very graphic manner.

The energy spectra of the two areas (using both row- and column-averaged shift and multiply) are shown in Figure 26. This spectra is a correlogram, which is the Fourier transform of the autocorrelation estimates. Several references [2, 8, 9, 10] show estimations of what the spectra should look like. Typically on such plots the energy is normalized by the product of the fluid viscosity (to the $\frac{5}{4}$) and the dissipation (to the quarter power), and the wave number is multiplied by an appropriate length scale (either the Taylor micro-scale or the Kolmogorov length scale). The result is a curve with a slope of -1 out to moderate wave numbers, and then a change to a slope of $-\frac{5}{3}$ for large wave numbers for wall bounded shear flows. In wakes, the slopes are expected to be similar. In an isotropic turbulence, the $-\frac{5}{3}$ slope dominates the wavenumber space [2]. This is shown schematically in Figure 27. The change in slope occurs at unity in both the dimensionless wavenumber and dimensionless energy. (The initial portion of the curve is nearly flat.)

In the present work, the values are not normalized, since it was unclear which length scale to use. None-the-less, on a log-log scale both normalizations produce an offset only, so the

slope of the curve will remain the same no matter which scale is used. The results show two distinct linear regions, with the slope for higher wave numbers more negative than at low wave numbers. At low wave numbers the slope for both digitized areas is roughly -1, in good agreement with predicted values. The above is true for wave numbers up to 0.2; at this point, there is another change in slope. The data become somewhat more noisy, also. These data appear to be accurate, since the large spike at the highest wave number corresponds to the Nyquist rate error in the scanner CCD array described in the Equipment section. At present, there is no explanation for the second change in slope. There is some offset between the two digitized areas, and this suggests (as shown above) different length scales in the two areas.

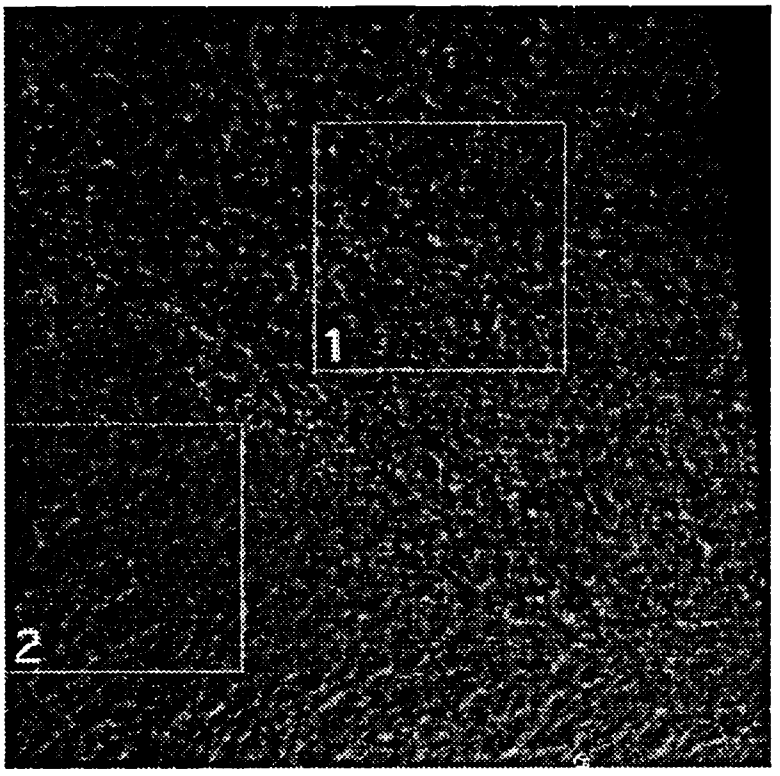

Figure 7: Digitized Shadowgraph, Areas Studied

Quantity†	Area One	Area Two
Minimum g	14	16
Maximum g	140	137
Number of g	127	122
Equivalent dB	44	43
Mean g	48	58
Variance	143	155
Standard Deviation	15.6	12.4
Skewness	4615	1579
†Term g is the gray scale value		

Table 1: Statistics for the Digitized Shadowgraphs

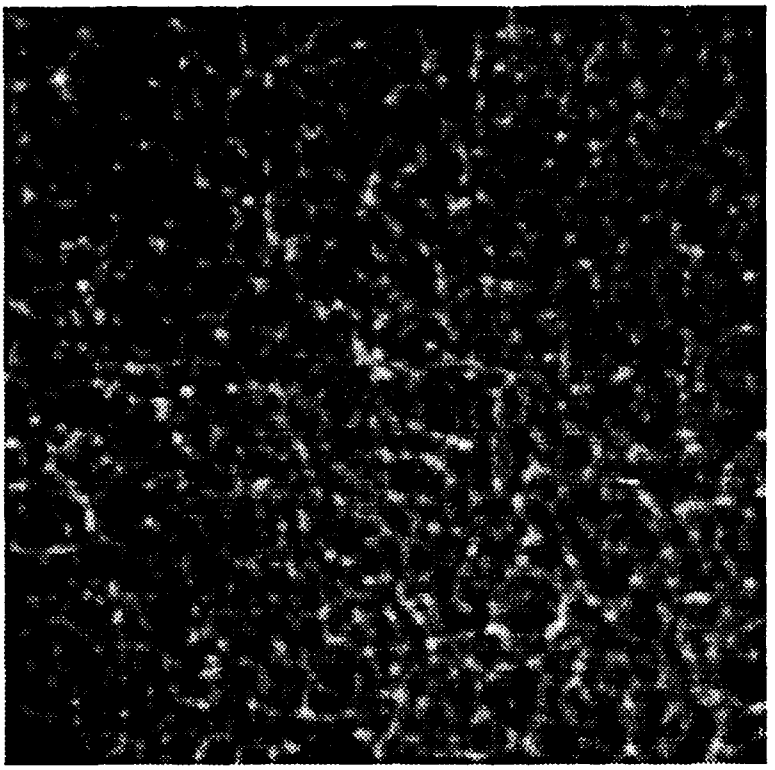

Figure 8: Area One, Expanded View

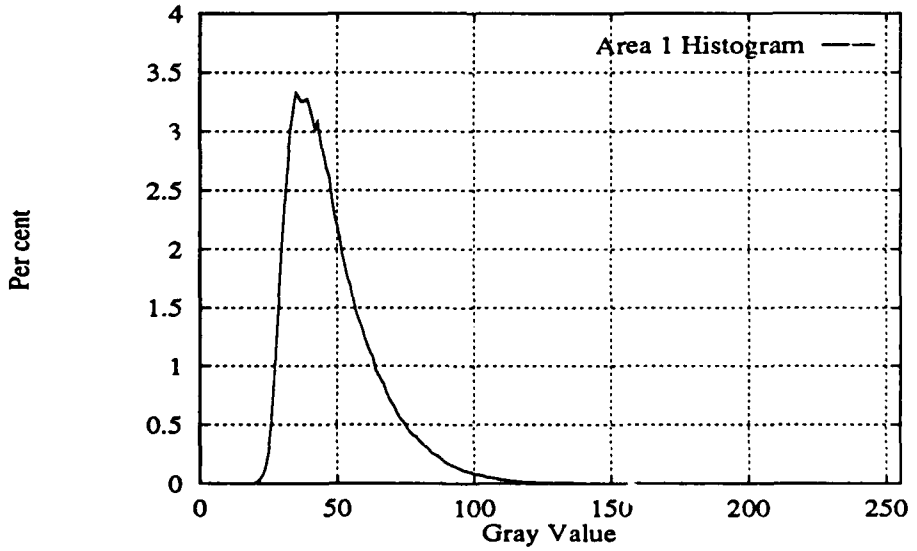

Figure 9: Histogram of Area One

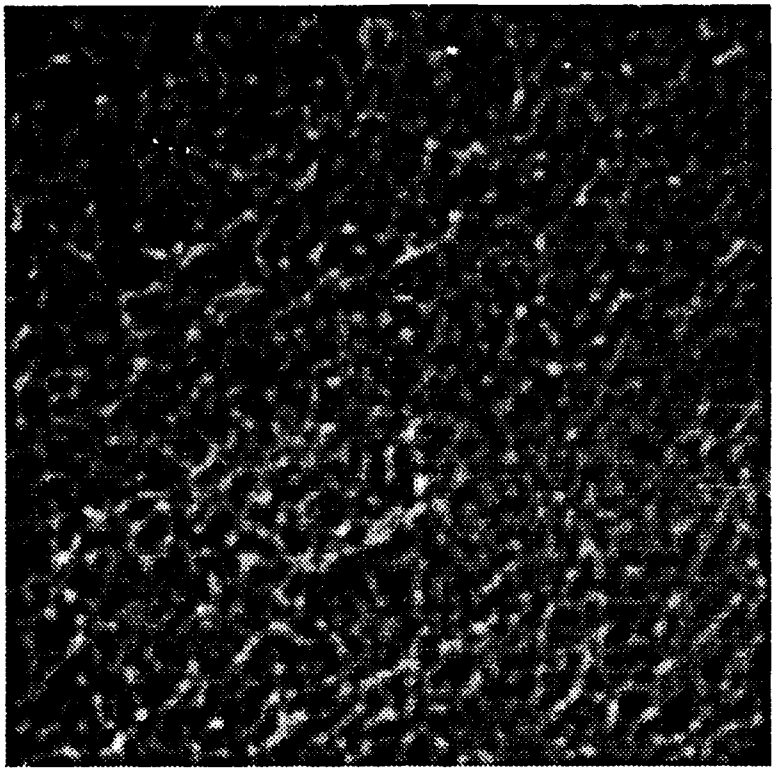

Figure 10: Area Two, Expanded View

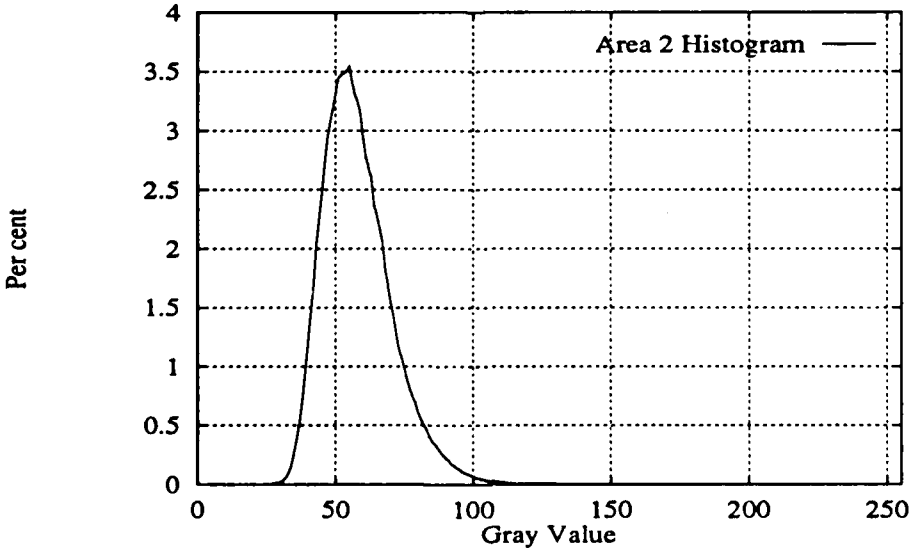

Figure 11: Histogram of Area Two

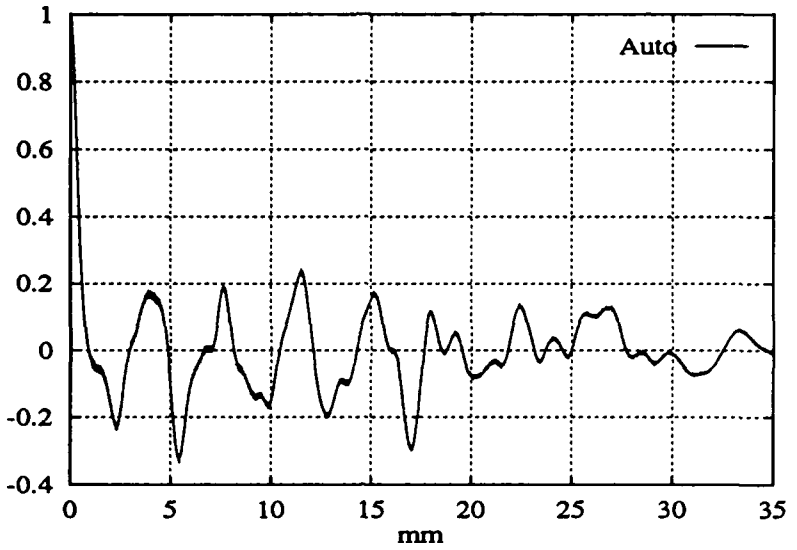

Figure 12: 1-D Autocorrelation, First Row in Area One

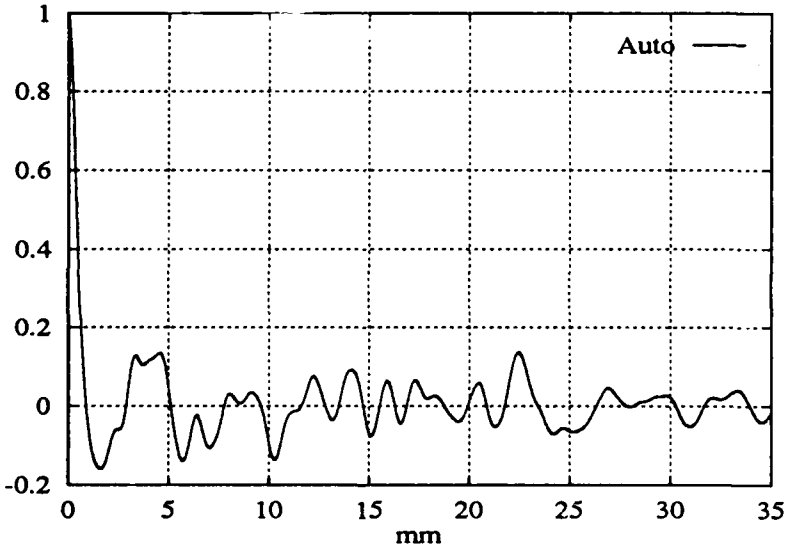

Figure 13: 1-D Autocorrelation, First Column in Area One

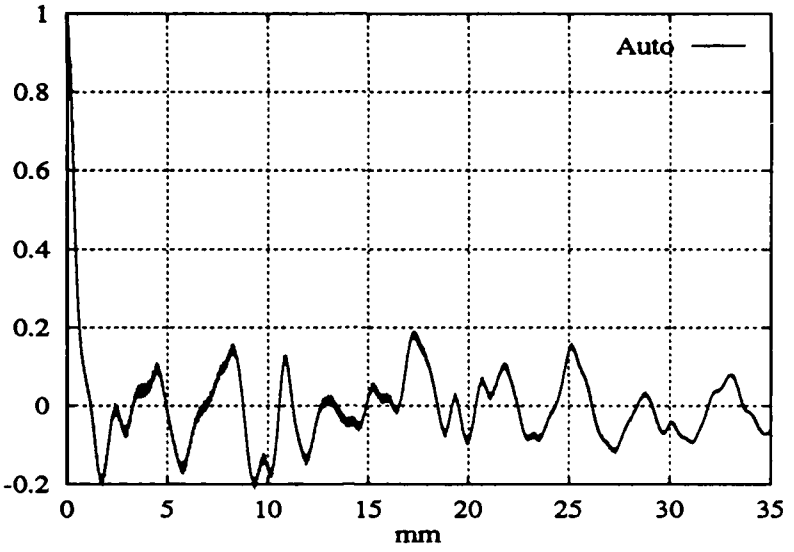

Figure 14: 1-D Autocorrelation, First Row in Area Two

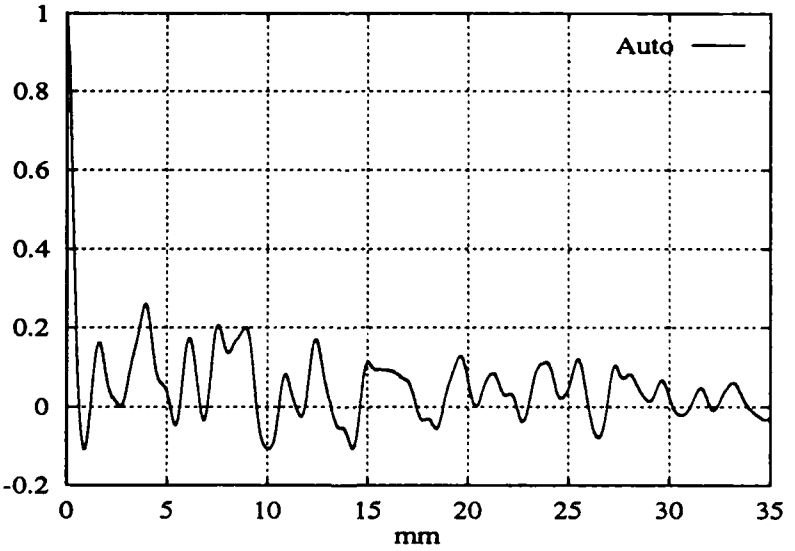

Figure 15: 1-D Autocorrelation, First Column in Area Two

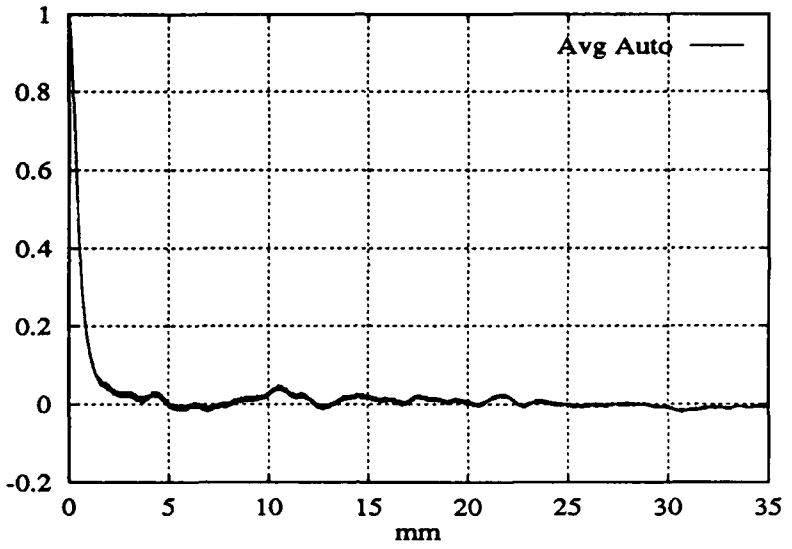

Figure 16: 1-D Autocorrelation, Row Average in Area One

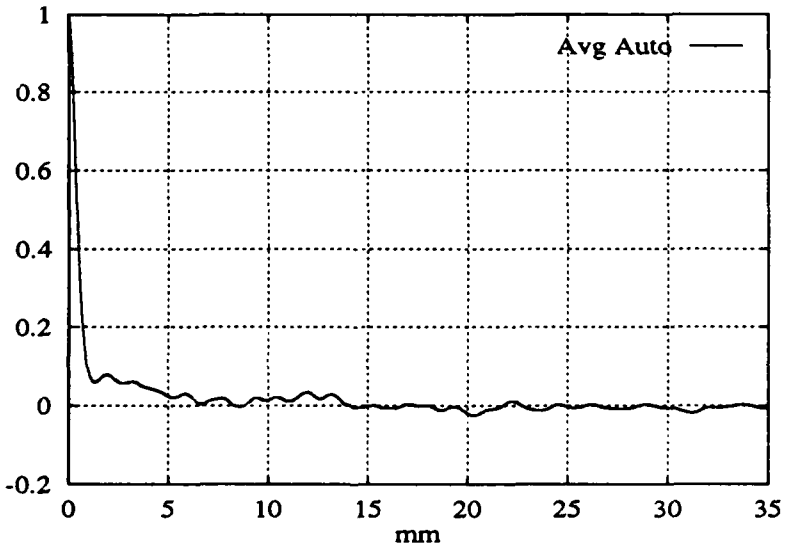

Figure 17: 1-D Autocorrelation, Column Average in Area One

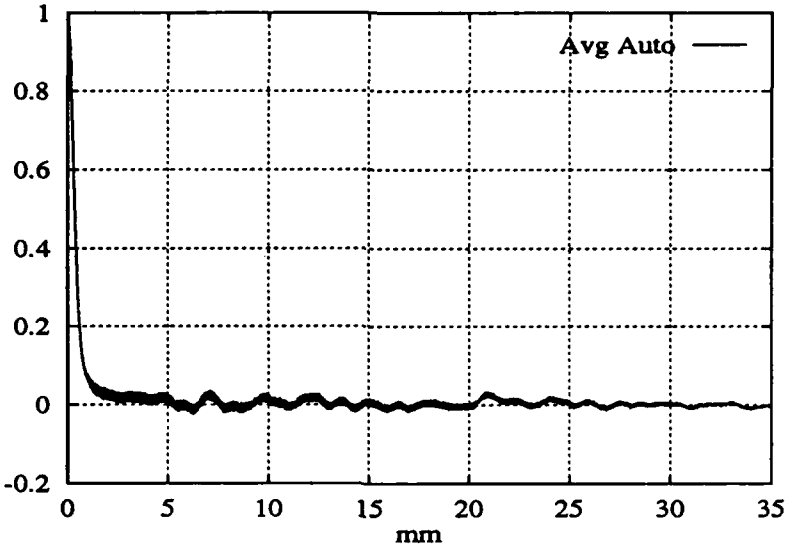

Figure 18: 1-D Autocorrelation, Row Average in Area Two

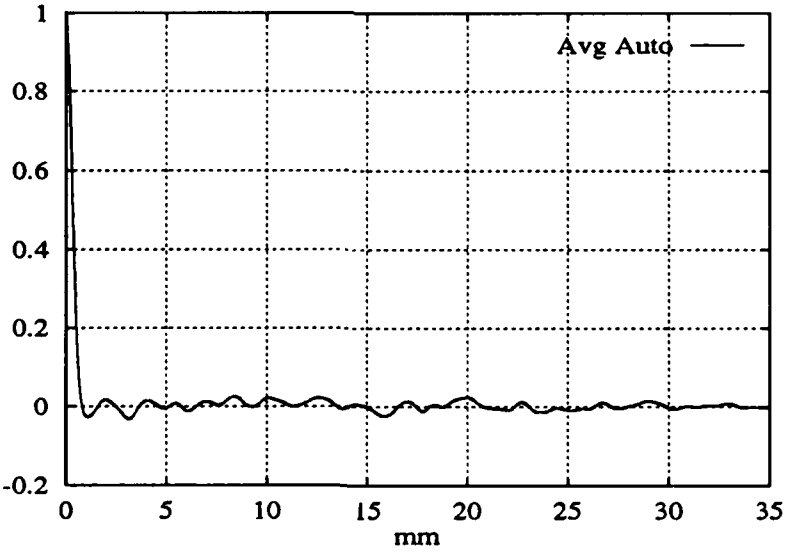

Figure 19: 1-D Autocorrelation, Column Average in Area Two

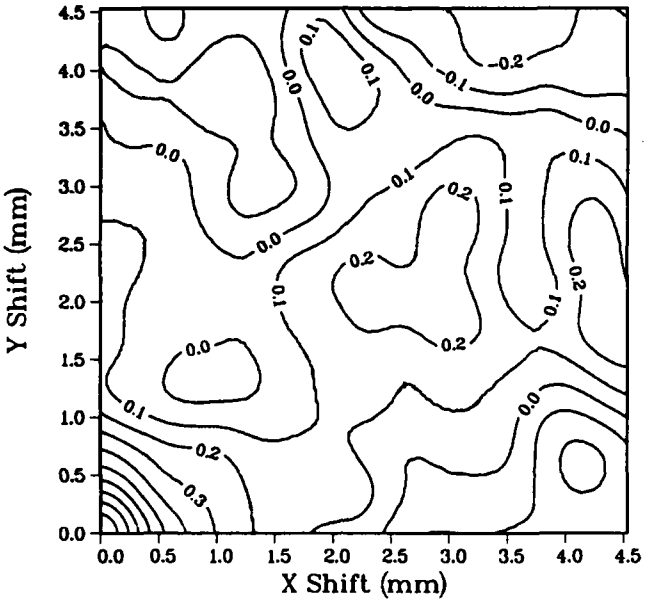

Figure 20: 2-D Autocorrelation Contours, Area One

Figure 21: 2-D Autocorrelation in Gray Scale, Area One

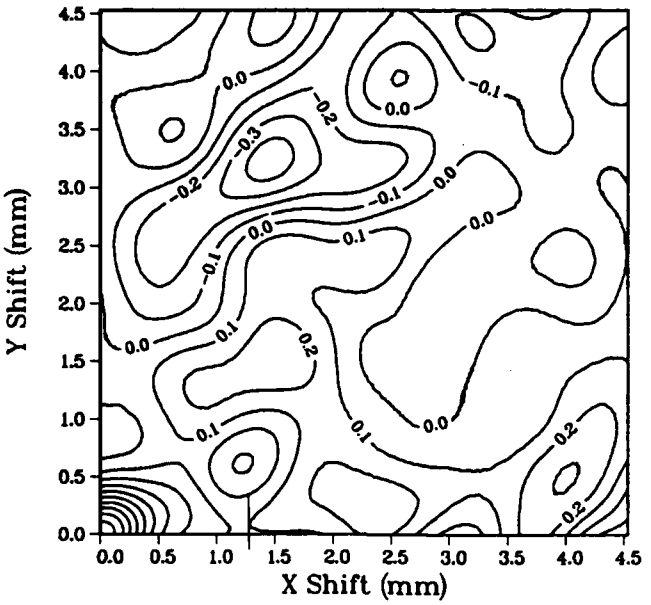

Figure 22: 2-D Autocorrelation Contours, Area Two

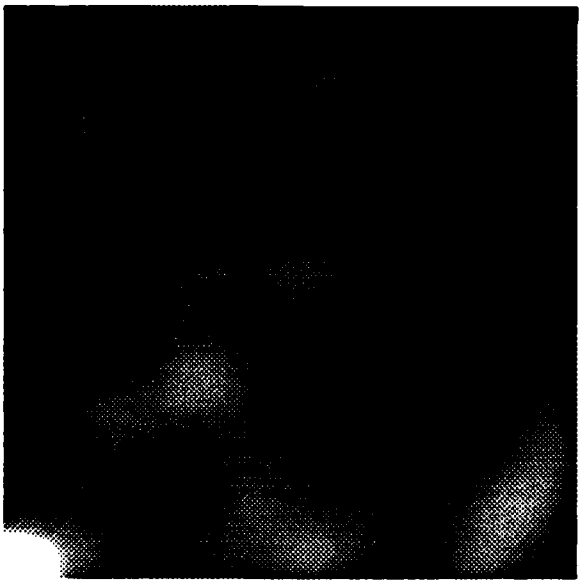

Figure 23: 2-D Autocorrelation in Gray Scale, Area Two

Figure 24: Circular Correlation of Five Degrees, Area One

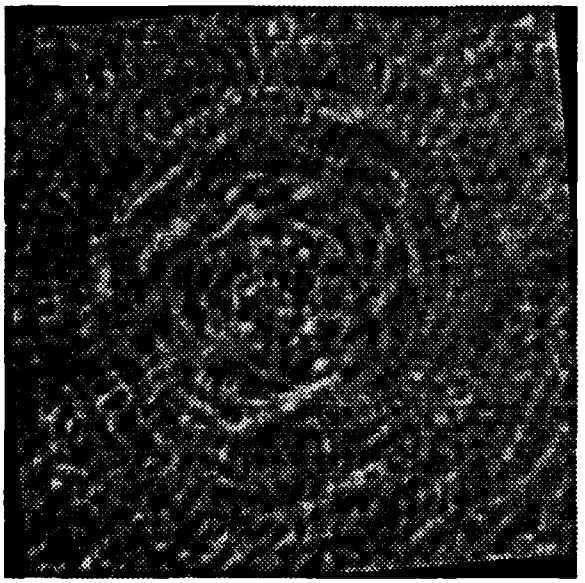

Figure 25: Circular Correlation of Five Degrees, Area Two

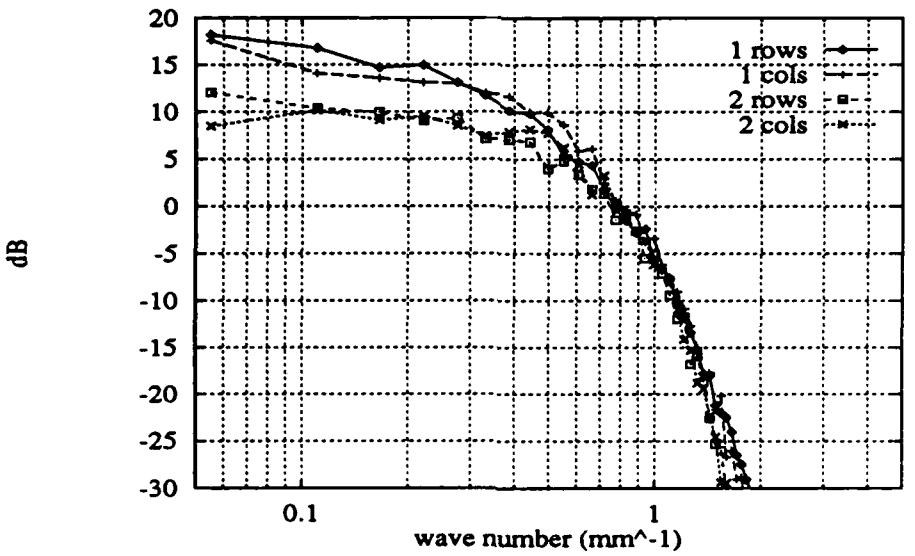

Figure 26: Energy Spectra of the Row and Column Averaged Data in Areas 1 and 2

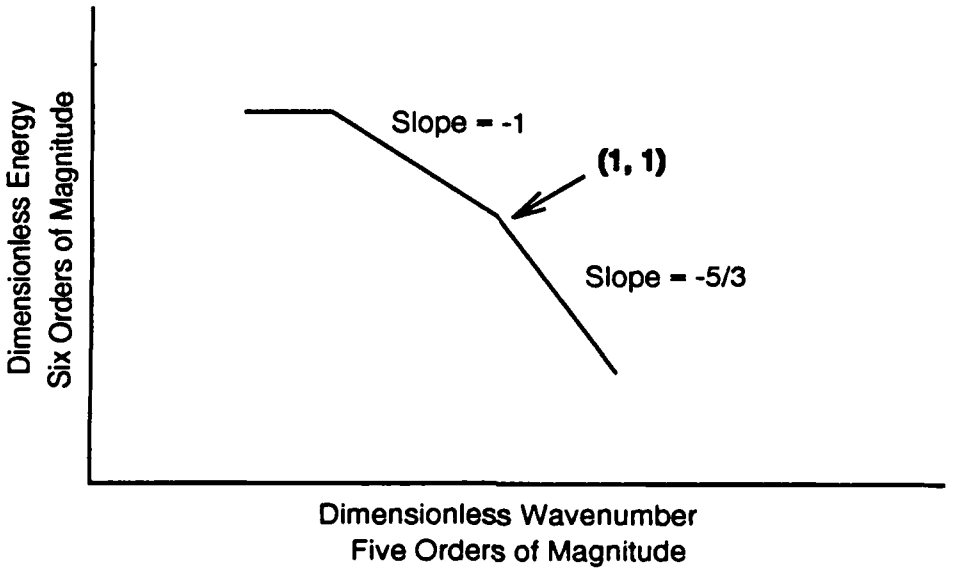

Figure 27: Schematic of the Energy Spectra for Wall Bounded Shear Flow

8 Conclusions and Future Work

The conclusions reached in this work are as follows:

- Discrete interrogation of shadowgraphs gives results that are nearly identical to analog techniques.
- Discrete interrogation is much faster than analog techniques and it allows the data to be manipulated easily.
- Further investigation should begin with a homogeneous, turbulent wake with known maximum length scales.
- Mathematical relations between length scales and the density fluctuations must be established.

The goal of this work was to help computational fluid mechanics by gaining knowledge about the scales of motion in a turbulent flow field. This first effort is far short of that goal, but establishes a collection of tools that may help to exploit ballistic range shadowgraphs for this purpose. There are three efforts that would enhance the technique without developing complicated three-dimensional image equipment.

First, a conditional averaging approach to the simple technique described in this report would give a better indication of the length scale. The conditions would pick the size of the area to be averaged such that the random nature of the flow field would not dominate the results and the small scale coherence could be traced.

Second, in an effort to study the far field wake or the wake at different angles of yaw, several mosaic stations could be set up to image the wake. The far field wake could be imaged by triggering three or four mosaic stations at the same time, thus capturing a significant portion of the wake in three or four locations. Triggering the stations as the projectile passed through would show the near field wake under different conditions and, using several assumptions and Taylor's theory, might allow approximations of three-dimensional structure.

Finally, a two slice mosaic station could be constructed to allow two shadowgraphs to be obtained at right angles. This might yield some information about the three-dimensional structure of the wake.

Computer	Compile Options	Shifts/sec	MFLOPS	× VAX
VAX 11/780	cc -O	.42	0.13	1.0
Sun 3/280	cc -O -f68881	.42	0.13	1.0
Sun 3/280	gcc -O	.70	0.22	1.7
Gould 9080	cc -O	1.35	0.43	3.2
VAX 6320	cc -O	1.71	0.55	4.1
Alliant FX/8	cc -O	1.72	0.55	4.1
SGI 4D/240	cc -03	8.90	2.80	21.0
Cray X-MP/48	cc	13.20	4.20	31.0
IBM R6000	cc -O	27.00	8.60	64.0
Cray 2	scc	189.00	60.00	450.0
Cray X-MP/48	cc -holevel_3 -hivdep	233.00	75.00	554.0
Cray X-MP/48	scc	345.00	110.00	821.0

Table 2: Two Dimensional Autocorrelation Computation Speed

Appendix A. Computational Speed

Most of the computations performed in this report were of a very simple nature; however, the volume of data involved demands substantial processing power. While a detailed comparison of different computers used in the laboratory is beyond the scope of this report, we present one example of the relative speeds of various machines for the typical kind of processing this report required.

The two dimensional autocorrelation involves point multiplying two copies of an image, one of which is shifted in the horizontal and/or vertical direction. The results of these multiplies are then summed together. A simple C program to compute this autocorrelation was written, the inner loop of which is essentially a vector dot product. In the report, 512 shifts in width and height (262144 total) were used, each multiplied and summed over an area of 512 by 512 samples. The total number of floating point adds and multiplies required is 137 billion.[4]

Table 2 compares the rates at which a selection of computers could perform a simple two dimensional autocorrelation. The type of computer, along with the compiler and options used is shown. The value of shifts per seconds is for a 400 by 400 sample area. Millions of floating point operations per second (MFLOPS) is found by multiplying the shifts per second by 0.32, as 320 thousand multiplies and adds are required for each shift. Finally, the speed normalized to that of the VAX 11/780 is shown. In all cases the computation was done using full precision (64 bit).

A few characteristics are worth pointing out. The Sun 3/280 is shown as speeding up by more than fifty per cent by the change in C compilers. The Cray X-MP also shows a near fifty per cent increase under different compilers. More interesting is the two cases of the Cray X-MP using cc. With the option to "ignore vector dependencies" the inner loop of the autocorrelation code vectorized and resulted in an 18 times speedup. This was typical

[4] Use of the Fast Fourier Transform to perform the autocorrelation could reduce the operation count by approximately a factor of fifty; but, the relative requirements discussed here still apply.

of several programs being applied to this data: the strictly scalar floating point speed of the X-MP was about 30 times a VAX 11/780, yet vectorization could result in another 20 to 30 fold speedup.

To put the scale of the above numbers in better perspective, consider the original two dimensional autocorrelations computed in this report. On the Sun 3/280 where the images were scanned, one autocorrelation would have taken over seven days of computer time. On the Cray X-MP/48, these could each be done in twenty minutes.

Appendix B. Turbulent Wake Flow

Wake flows show similarity in patterns at different sections downstream of the projectile. Self-preservation of these patterns moving downstream with the main flow is because the un-bounded turbulent region in the wake is narrow with respect to its length. Streamwise speed is at least an order of magnitude greater than transverse speed, but the turbulence intensity is only twice as great in the streamwise direction. In this condition, changes in flow patterns are not exaggerated in the streamwise direction (hence, they are "self-preserving"), but are strongly dependent on their history [2].

Self-preservation would only hold for the middle range of wavenumbers of the turbulence (see Section 7) without production of turbulence; a grid-turbulence in a wind tunnel is an example of self-preservation in a decaying turbulent flow field. With turbulence production, self-preservation might not occur, since the scales of motion would be dependent on the turbulence production. In a wake, however, the production is dependent on the turbulence produced upstream and transported downstream by diffusion and convection [8]. Thus, self-preservation might be expected to occur and there is strong evidence of this in the similarity of turbulence patterns in the image of wake flows.

Similarity in a flow field's patterns means that all velocities are represented by one characteristic velocity and the scales of motion are represented by a characteristic length. Using the similarity assumption, which is strongly dependent on self-preservation, the equations of motion for a turbulent wake can be simplified. Unfortunately, most experimental measurements [2] in axi-symmetric wake flows suggest that similarity is at best "incomplete," and this is true only in the far field wake.

Given:

1. the difficulty in developing adequate turbulence models to compute the wake flow field of artillery and direct-fire projectiles;
2. the inability to simplify the equations of motion in the near wake;
3. the lack of copious experimental data (as in wall-bounded flows); and
4. the lack of development of experimental techniques that could be used to investigate projectile wake flows

it is very important to develop the techniques and to obtain experimental measurements of turbulence quantities in the wake.

References

[1] L. S. G. Kovasznay. Technique for the optical measurement of turbulence in a high speed flow. *Heat Transfer and Fluid Mechanics Institute Journal*, 211–222, March 1949.

[2] J. O. Hinze. *Turbulence.* McGraw-Hill, New York, 1975.

[3] B. S. Baldwin and H. Lomax. Thin layer approximation and algebraic model for separated turbulent flows. *Proceedings of the AIAA 16th Aerospace Sciences Meeting*, 157–172, January 1978.

[4] Jr. W. K. Rogers. *The Transonic Free Flight Range.* Technical Report Report Number 1044, U.S. Army Ballistic Research Laboratory, APG, MD, June 1958. (AD 200177).

[5] H. W. Liepmann and A. Roshko. *Elements of Gasdynamics.* John Wiley and Sons, Inc., New York, 1957.

[6] F. J. Weinberg. *Optics of Flames.* Butterworths, Washington, 1963.

[7] M. S. Uberoi and L. S. G. Kovasznay. Analysis of turbulent density fluctuations by the shadow method. *Journal of Applied Physics*, 26(1):19–24, January 1955.

[8] H. Tennekes and J. L. Lumley. *A First Course in Turbulence.* MIT Press, London, 1972.

[9] A. A. Townsend. *The Sturcture of Turbulent Shear Flow.* Cambridge University Press, Cambridge, 1976.

[10] F. S. Sherman. *Viscous Flow.* McGraw-Hill, New York, 1990.

INTENTIONALLY LEFT BLANK.

No. of Copies	Organization
2	Administrator Defense Technical Info Center ATTN: DTIC-DDA Cameron Station Alexandria, VA 22304-6145
1	Commander U.S. Army Materiel Command ATTN: AMCDRA-ST 5001 Eisenhower Avenue Alexandria, VA 22333-0001
1	Commander U.S. Army Laboratory Command ATTN: AMSLC-DL 2800 Powder Mill Road Adelphi, MD 20783-1145
2	Commander U.S. Army Armament Research, Development, and Engineering Center ATTN: SMCAR-IMI-I Picatinny Arsenal, NJ 07806-5000
2	Commander U.S. Army Armament Research, Development, and Engineering Center ATTN: SMCAR-TDC Picatinny Arsenal, NJ 07806-5000
1	Director Benet Weapons Laboratory U.S. Army Armament Research, Development, and Engineering Center ATTN: SMCAR-CCB-TL Watervliet, NY 12189-4050
(Unclass. only) 1	Commander U.S. Army Armament, Munitions and Chemical Command ATTN: AMSMC-IMF-L Rock Island, IL 61299-5000
1	Director U.S. Army Aviation Research and Technology Activity ATTN: SAVRT-R (Library) M/S 219-3 Ames Research Center Moffett Field, CA 94035-1000

No. of Copies	Organization
1	Commander U.S. Army Missile Command ATTN: AMSMI-RD-CS-R (DOC) Redstone Arsenal, AL 35898-5010
1	Commander U.S. Army Tank-Automotive Command ATTN: ASQNC-TAC-DIT (Technical Information Center) Warren, MI 48397-5000
1	Director U.S. Army TRADOC Analysis Command ATTN: ATRC-WSR White Sands Missile Range, NM 88002-5502
1	Commandant U.S. Army Field Artillery School ATTN: ATSF-CSI Ft. Sill, OK 73503-5000
(Class. only) 1	Commandant U.S. Army Infantry School ATTN: ATSH-CD (Security Mgr.) Fort Benning, GA 31905-5660
(Unclass. only) 1	Commandant U.S. Army Infantry School ATTN: ATSH-CD-CSO-OR Fort Benning, GA 31905-5660
1	Air Force Armament Laboratory ATTN: WL/MNOI Eglin AFB, FL 32542-5000
	Aberdeen Proving Ground
2	Dir, USAMSAA ATTN: AMXSY-D AMXSY-MP, H. Cohen
1	Cdr, USATECOM ATTN: AMSTE-TD
3	Cdr, CRDEC, AMCCOM ATTN: SMCCR-RSP-A SMCCR-MU SMCCR-MSI
1	Dir, VLAMO ATTN: AMSLC-VL-D
10	Dir, BRL ATTN: SLCBR-DD-T

No. of Copies	Organization
2	Commander U.S. Army Armament Research, Development, and Engineering Center ATTN: SMCAR-FSP-A R. Kline H. Hudgins Picatinny Arsenal, NJ 07806-5000
1	Commander U.S. Army Missile Command ATTN: AMSMI-RDK, W. Dahlke Redstone Arsenal, AL 35898-5010
1	Commander Naval Surface Warfare Center ATTN: Dr. W. Yanta Aerodynamics Branch K-24, Bldg. 402-12 White Oak Laboratory Silver Spring, MD 20910
1	Army High Performance Computing Research Center University of Minnesota ATTN: Paul Woodward FMC Technology Center 1300 South Second Street Minneapolis, MN 55454
2	Rockwell International Science Center ATTN: Dr. S. Chakravarthy Dr. U. Goldberg 1049 Camino Dos Rios P.O. Box 1085 Thousand Oaks, CA 91360
1	Georgia Institute of Technology The George W. Woodruff School of Mechanical Engineering ATTN: Dr. G.P. Neitzel Atlanta, GA 30332-0405

USER EVALUATION SHEET/CHANGE OF ADDRESS

This laboratory undertakes a continuing effort to improve the quality of the reports it publishes. Your comments/answers below will aid us in our efforts.

1. Does this report satisfy a need? (Comment on purpose, related project, or other area of interest for which the report will be used.) _____

2. How, specifically, is the report being used? (Information source, design data, procedure, source of ideas, etc.) _____

3. Has the information in this report led to any quantitative savings as far as man-hours or dollars saved, operating costs avoided, or efficiencies achieved, etc? If so, please elaborate. _____

4. General Comments. What do you think should be changed to improve future reports? (Indicate changes to organization, technical content, format, etc.) _____

BRL Report Number BRL-MR-3922 Division Symbol _____

Check here if desire to be removed from distribution list. ____

Check here for address change. ____

Current address: Organization _____
Address _____

DEPARTMENT OF THE ARMY
Director
U.S. Army Ballistic Research Laboratory
ATTN: SLCBR-DD-T
Aberdeen Proving Ground, MD 21005-5066

OFFICIAL BUSINESS

BUSINESS REPLY MAIL
FIRST CLASS PERMIT No 0001, APG, MD

Postage will be paid by addressee.

Director
U.S. Army Ballistic Research Laboratory
ATTN: SLCBR-DD-T
Aberdeen Proving Ground, MD 21005-5066

NO POSTAGE
NECESSARY
IF MAILED
IN THE
UNITED STATES